Compressed-Sensing Approach to Magnetic-Flux Map Acquisition with Experimental Validation

Patkar, Abhishek; Wang, Yebin; Goldsmith, Abraham; Liu, Dehong; Youcef-Toumi, Kamal

TR2026-120 September 09, 2026

Abstract

An accurate magnetic model is essential for highperformance control of electric motors because it characterizes magnetic flux as a nonlinear function of the stator current. However, both acquiring and using magnetic flux maps can be time-consuming, making them unsuitable for low-latency control applications. To address this limitation, we propose a compressedsensing-based approach that reconstructs magnetic flux maps from a limited set of randomly sampled data points. Experiments are conducted on a permanent-magnet machine to validate the proposed method. Extensive simulation and experimental results demonstrate that, by exploiting the sparsity of flux maps, the proposed approach can accurately reconstruct the maps using only 25% of the full experimental samples, thereby significantly reducing the acquisition time.

International Conference on Electrical Machines (ICEM) 2026

Compressed-Sensing Approach to Magnetic-Flux Map Acquisition with Experimental Validation

Abhishek Patkar
Massachusetts Institute of Technology
Cambridge, MA, USA
patkar2@mit.edu

Yebin Wang
Mitsubishi Electric Research Laboratories (MERL)
Cambridge, MA, USA
yebinwang@merl.com

Abraham Goldsmith
Mitsubishi Electric Research Laboratories (MERL)
Cambridge, MA, USA
goldsmith@merl.com

Dehong Liu
Mitsubishi Electric Research Laboratories (MERL)
Cambridge, MA, USA
liudh@merl.com

Kamal Youcef-Toumi
Massachusetts Institute of Technology
Cambridge, MA, USA
youcef@mit.edu

***Abstract*—An accurate magnetic model is essential for high-performance control of electric motors because it characterizes magnetic flux as a nonlinear function of the stator current. However, both acquiring and using magnetic flux maps can be time-consuming, making them unsuitable for low-latency control applications. To address this limitation, we propose a compressed-sensing-based approach that reconstructs magnetic flux maps from a limited set of randomly sampled data points. Experiments are conducted on a permanent-magnet machine to validate the proposed method. Extensive simulation and experimental results demonstrate that, by exploiting the sparsity of flux maps, the proposed approach can accurately reconstruct the maps using only 25% of the full experimental samples, thereby significantly reducing the acquisition time.**

***Index Terms*—Compressed sensing, flux maps, spatial harmonics, motor control**

I. Introduction

With the advent of data-driven control and an increasing demand for precise motor operation, increasingly sophisticated control strategies such as maximum torque per ampere (MTPA), maximum torque per volt (MTPV), signal-injection sensorless control, and model predictive control (MPC) have been proposed [1]–[3]. Such advanced control strategies require an accurate magnetic model to achieve the desired control performance.

For a 2D flux map, the magnetic model characterizes the magnetic flux as a function of stator current in a selected reference frame; for a 3D flux map, it additionally depends on rotor angular position to capture spatial harmonics [4], [5]. For instance, in the d-q reference frame, the magnetic model for IPMs and SynRMs is highly nonlinear owing to saturation and cross-saturation effects [6]–[9].

To characterize magnetic-model nonlinearity, significant research effort has been devoted to developing analytical magnetic models [10]–[13]. For example, Qu *et al.* [12] proposed a polynomial model to capture nonlinear effects, treating the d-q axis currents as state variables and the flux linkages as independent variables.

Although the magnetic model can be simulated using Finite Element Analysis (FEA) [14], the FEA-based model needs to be validated through experiments to guarantee its accuracy. Therefore, it is crucial to conduct experiments to acquire the magnetic flux at different current operating points.

However, experimental flux-map identification faces two major challenges. First, it is very time-consuming to collect enough data for an accurate flux model across the operating range of the motor under test [15]. Second, for permanent-magnet machines, long-duration experiments may cause demagnetization due to overheating. It is thus desirable to reduce the number of tests conducted without compromising the accuracy of the acquired flux map.

In this paper, we investigate a compressed-sensing-based approach to flux map acquisition [16]. The proposed approach is validated on both publicly available simulation data and privately collected experimental data using a well-designed experimental platform.

II. Flux map acquisition via Compressed Sensing

During flux-map acquisition, the flux map is treated as a compressible signal, meaning that it can be accurately represented by a small number of active modes in an appropriate basis, such as a Fourier basis, a wavelet basis, or another learned dictionary.

This work was done when Abhishek was an intern at MERL.

A. Compressed Sensing

Without loss of generality, let $x \in \mathbb{R}^n$ be a compressible signal, meaning that there exists a basis $\mathbf{\Psi}$ such that

$$x = \mathbf{\Psi} s, \tag{1}$$

where $s \in \mathbb{R}^n$ can be approximated using a sparse vector. If s has at most K nonzero elements, x is K-sparse. The measurements $y \in \mathbb{R}^p$ with $(K < p \ll n)$ are given by

$$y = \mathbf{C} x, \tag{2}$$

where $\mathbf{C} \in \mathbb{R}^{p \times n}$ is the measurement matrix. Compressed sensing seeks to find a sparse vector $\hat{s}$ such that

$$\hat{s} = \arg\min_s ||s||_0 \quad \text{subject to } y = \mathbf{C\Psi} s, \tag{3}$$

where $|| \cdot ||_0$ is the ℓ_0 norm, i.e., the cardinality of s. The non-convex optimization in (3) may be relaxed to a ℓ_1-minimization problem as

$$\hat{s} = \arg\min_s ||s||_1 \quad \text{subject to } y = \mathbf{C\Psi} s, \tag{4}$$

where $|| \cdot ||_1$ is the ℓ_1 norm given by $||s||_1 = \sum_{k=1}^{n} |s_k|$ provided that

1) $\mathbf{C}$ is incoherent with respect to $\mathbf{\Psi}$,
2) the number of measurements p is sufficiently large, i.e., $p \approx \mathcal{O}\left(K \log\left(\frac{n}{K}\right)\right)$ [17].

In this paper, to satisfy the incoherence property, we use random samples of the flux map. We also study the variation of reconstruction error with the number of measurements.

An alternative formulation is given by

$$\hat{s} = \arg\min_s \frac{1}{2} ||y - \mathbf{C\Psi} s||_2^2 + \lambda ||s||_1, \tag{5}$$

where $\lambda \geq 0$ is a regularization parameter weighting the importance of a sparse solution. In this paper, the formulation presented in (5) is used.

B. Flux Map Reconstruction

This subsection applies the formulation in (1)-(5) to 3D flux-map reconstruction. Let ϕ be the true unknown discrete flux map with dimensions $N_1 \times N_2 \times N_3$. Let Φ be the corresponding Fourier transform.

Let y be the p-vector of the measured samples. Let $\Omega \subset \{1, \ldots, n\}$ denote the set of measured entries of the vectorized flux map ϕ_u, where $|\Omega| = p$ and $p \ll n$. The sampling operation can be represented by a row-selection matrix $\mathbf{C}_\Omega \in \mathbb{R}^{p \times n}$, whose rth row is the standard basis vector $e_{\Omega_r}^T$. Thus, y is given by

$$y = \mathbf{C}_\Omega \phi_u. \tag{6}$$

The corresponding zero-padded flux-map vector is

$$(\phi_{zp})_u = \mathbf{C}_\Omega^+ y. \tag{7}$$

Since $\mathbf{C}_\Omega$ consists of selected rows of the identity matrix and $\mathbf{C}_\Omega \mathbf{C}_\Omega^T = \mathbf{I}_p$, its pseudo-inverse is $\mathbf{C}_\Omega^+ = \mathbf{C}_\Omega^T$. The vector $\mathbf{C}_\Omega^+ y$ places measured samples at indices Ω and zeros elsewhere.

Since $\phi_u = \mathbf{\Psi} s$, the compressed-sensing reconstruction problem is formulated as

$$\hat{s} = \arg\min_s \frac{1}{2} \|y - \mathbf{C}_\Omega \mathbf{\Psi} s\|_2^2 + \lambda \|s\|_1. \tag{8}$$

Once the sparse Fourier coefficients are obtained by solving (8), the flux map is reconstructed as

$$\hat{\phi}_u = \mathbf{\Psi} \hat{s}. \tag{9}$$

To construct the Fourier basis matrix $\mathbf{\Psi}$, we first define the $N \times N$ DFT matrix $\boldsymbol{W}$ for an N-sample 1D signal as

$$\boldsymbol{W}_N[c, d] = W_N^{cd},$$

where $W_N = e^{-\frac{j2\pi}{N}}$. The corresponding inverse DFT matrix is given by

$$\boldsymbol{W}_N^{-1}[g, h] = \frac{1}{N} \bar{W}_N^{gh},$$

where $\bar{W}_N = e^{\frac{j2\pi}{N}}$. The relationship between Φ_u and ϕ_u is given by

$$\Phi_u = (\boldsymbol{W}_{N_3} \otimes \boldsymbol{W}_{N_2} \otimes \boldsymbol{W}_{N_1}) \phi_u, \tag{10}$$

where $\otimes$ is the Kronecker product between two matrices. The Fourier basis matrix $\mathbf{\Psi}$ is obtained as the inverse of the forward transformation in (10). Thus, for the 3D case, we have

$$\mathbf{\Psi} = \boldsymbol{W}_{N_3}^{-1} \otimes \boldsymbol{W}_{N_2}^{-1} \otimes \boldsymbol{W}_{N_1}^{-1} \tag{11}$$

The $\mathbf{\Psi}$ matrix for the 2D case can be computed analogously. It can be readily seen that $\mathbf{\Psi}^{-1} = (\boldsymbol{W}_{N_3} \otimes \boldsymbol{W}_{N_2} \otimes \boldsymbol{W}_{N_1})$. While (11) defines the Fourier basis matrix for mathematical completeness, in practice, Algorithm 1 uses the FFT and inverse FFT for efficient implementation.

C. Algorithm

This subsection describes the method used to reconstruct the flux map from limited random samples. To solve the optimization problem given in (8), a soft-thresholding-based iterative algorithm is used. The measured sample vector y is first embedded into the n-dimensional flux-map vector space as $(\hat{\phi}_1)_u = \mathbf{C}_\Omega^+ y$, which serves as the zero-padded initial estimate $\hat{\phi}_1$. At each iteration, the present flux-map estimate is transformed into the Fourier domain using the FFT. Soft thresholding is then applied to the Fourier coefficients to promote sparsity. After applying the inverse FFT to the thresholded Fourier coefficients, an intermediate flux-map vector $(\tilde{\phi}_{i+1})_u$ is obtained. Data consistency is then enforced by projecting this intermediate estimate onto the affine set of vectors matching the measurements $\{z : \mathbf{C}_\Omega z = y\}$. This projection is implemented as $(\hat{\phi}_{i+1})_u \leftarrow (\mathbf{I} - \mathbf{C}_\Omega^+ \mathbf{C}_\Omega)(\tilde{\phi}_{i+1})_u + \mathbf{C}_\Omega^+ y$. Here $(\mathbf{I} - \mathbf{C}_\Omega^+ \mathbf{C}_\Omega)$ preserves unmeasured entries, while $\mathbf{C}_\Omega^+ y$ restores the measured entries. For a row-selection matrix, this update simply restores the measured entries and leaves the unmeasured entries from the inverse FFT step. The iterative algorithm runs until convergence, that is, until the relative change between the two most recent reconstructions is below ϵ. The final iterate is returned as the reconstructed flux map.

The soft-thresholding function is defined as

$$S(u,\lambda) = \begin{cases} 0 & \text{if } |u| \le \lambda \\ \frac{|u|-\lambda}{|u|}u & \text{if } |u| > \lambda. \end{cases} \tag{12}$$

Here $|\cdot|$ denotes the absolute value and the threshold λ is the regularizing parameter used in (8). The threshold λ is empirically tuned. Initially, the threshold may be set to 5% of the maximum DFT coefficient of ϕ_{zp}.

Algorithm 1 Flux map reconstruction using CS

Input: $y, \mathbf{C}_\Omega, \lambda, \epsilon$
Procedure:

Initialize $i \leftarrow 1$, $(\hat{\phi}_0)_u \leftarrow \mathbf{0}$
$(\hat{\phi}_1)_u \leftarrow \mathbf{C}_\Omega^+ y$
while $\frac{||\hat{\phi}_i - \hat{\phi}_{i-1}||_2}{||\hat{\phi}_i||_2} \ge \epsilon$ **do**
    $(\hat{\Phi}_i)_u \leftarrow \mathbf{\Psi}^{-1}(\hat{\phi}_i)_u$, ▷ To Fourier domain
    $(\Phi_{i+1})_u \leftarrow S((\hat{\Phi}_i)_u, \lambda)$ ▷ Promote sparsity
    $(\tilde{\phi}_{i+1})_u \leftarrow \mathbf{\Psi}(\Phi_{i+1})_u$ ▷ Inverse FFT
    $(\hat{\phi}_{i+1})_u \leftarrow (\mathbf{I} - \mathbf{C}_\Omega^+\mathbf{C}_\Omega)(\tilde{\phi}_{i+1})_u + \mathbf{C}_\Omega^+ y$ ▷ Data consistency
    $i \leftarrow i+1$
end while
Output: $\hat{\phi} \leftarrow \hat{\phi}_i$

III. Simulation

To demonstrate the effectiveness of the proposed approach, we first evaluate it on simulated 3D flux maps.

The THOR dataset is used for the simulation study [18]. At every (I_d, I_q) grid point, we use only nine random samples over $[0, 2\pi]$. Algorithm 1 is then applied to reconstruct the 3D flux map. Fig. 1(a) illustrates the true flux variation, the random samples used, and the reconstructed q-axis flux-map variation with respect to θ at a fixed (I_d, I_q) grid point. Fig. 1(b) shows the corresponding quantities for the d-axis. To highlight the reconstruction using limited sampling, we also include results of linear interpolation and cubic spline interpolation of 9 equally spaced samples. Figs. 1(a) and 1(b) show that the CS-reconstructed flux maps match the spatial harmonic variation very well, while the interpolation-based methods fail to capture the pattern of spatial harmonics.

To further compare their performance quantitatively, the root-mean-squared errors (RMSEs) between the true flux maps and reconstructions are computed. The RMSEs between the true flux maps and the CS reconstructions are 0.0011 and 0.0009 for the q- and d-axes, respectively. The RMSEs between the true flux maps and the linear-interpolation flux maps are 0.0053 and 0.0043 for the q- and d-axes, respectively. Thus, the CS reconstruction reduces the error by a factor of approximately 5 in both the q- and d-axes. From Fig. 1 and the low RMSEs of CS-reconstructed flux maps, it can be concluded that the spatial harmonic behavior at different values of (I_d, I_q) can be modeled using a small number of 3D Fourier coefficients. The compressed-sensing-based approach reconstructs the 3D flux map using only a few random samples along θ at each grid point (I_d, I_q). These results demonstrate that the proposed CS-based approach captures spatial harmonics more accurately than interpolation-based reconstruction under limited sampling. Additional simulation studies, including a sensitivity analysis of the number of randomly sampled measurement points, are available in [16].

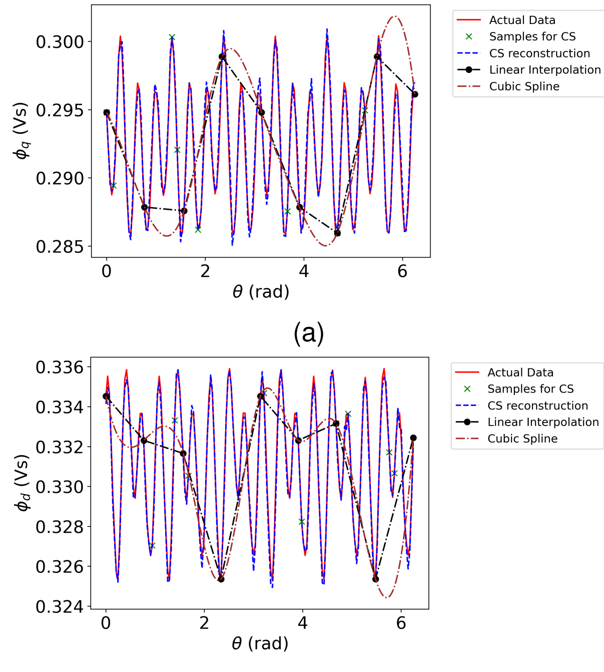

Fig. 1: q- and d-axis flux variation with θ at a particular (I_d, I_q) grid point. (a) Variation of ϕ_q with θ at $I_d = 39.7$ A, $I_q = 17.6$ A. (b) Variation of ϕ_d with θ at $I_d = 39.7$ A, $I_q = 17.6$ A.

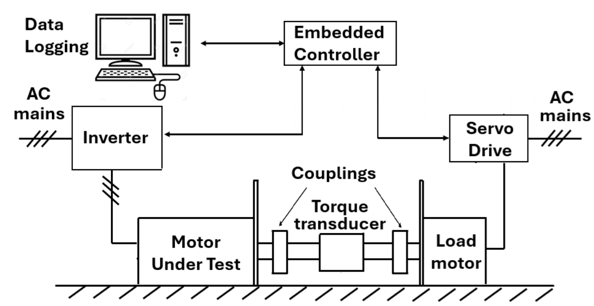

Fig. 2: Hardware setup schematic.

IV. Experimental Results

A. Hardware Setup

Fig. 2 shows a schematic of the experimental setup used to acquire the flux maps, and Fig. 3 shows photographs of the experimental hardware. An interior permanent-magnet (IPM) synchronous motor made by Marathon Motors is used as the motor under test (MUT). A servomotor manufactured by Mitsubishi Electric is utilized as the load motor. Table I

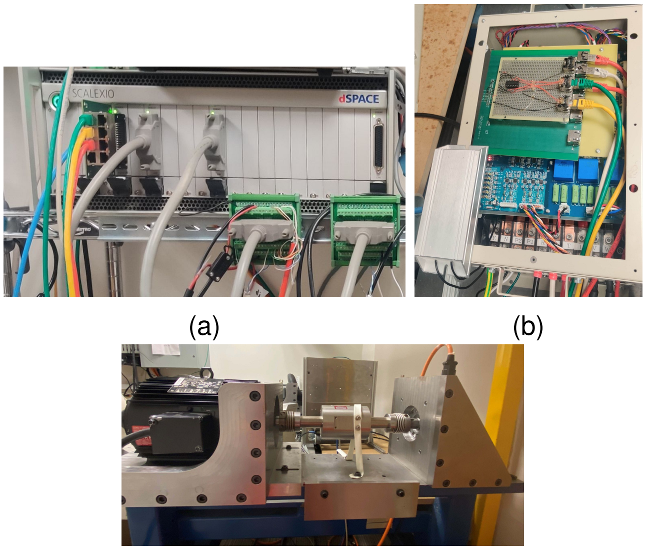

(a) (b) (c)

Fig. 3: Experimental devices. (a) dSPACE SCALEXIO lab box embedded controller. (b) Myway MWINV-2022B Inverter. (c) MUT and servomotor configuration.

TABLE I
MOTOR PARAMETERS

Parameter	Motor Under Test	Load Motor
Type	IPM	Servomotor
Model Name	184TPFRB10214A	HF-SP202K
Rated Power (kW)	3.7	2
Rated Speed (rpm)	1800	2000
Rated Torque (Nm)	19.8	9.55
Rated Current (A)	5.8	10

provides the relevant specifications for these two motors. A dSPACE SCALEXIO lab box, shown in Fig. 3(a), is used as the embedded controller for vector control of the IPM and speed control of the servomotor. The closed-loop rate for vector control of the IPM is 10 kHz. A Myway inverter model MWINV-2022B, shown in Fig. 3(b), is utilized as the drive inverter for the MUT. The rated output power of the inverter is 20.2 kW, with a rated voltage of 200 V and a rated current of 58.4 A. LEM IT 60-S ULTRASTAB current transducers are used to measure the phase currents. Fig. 3(c) illustrates the MUT and load motor configuration.

The load motor is commanded to regulate the shaft speed. The selected speed provides a good tradeoff: it is sufficiently high to obtain a good signal-to-noise ratio of V_d and V_q and low enough to have negligible iron and PM loss [15]. Note that the power of the load motor is lower than that of the motor under test, as shown in Table I. To explore the flux map at full rated motor current, the test is conducted at one third of the MUT rated speed.

B. Measurement Procedure

In an ideal configuration, the rotor angular position would be measured using a dedicated position sensor such as a resolver or encoder. However, because such sensors were unavailable in our experimental setup, a model-based flux observer was implemented to estimate the rotor angle. Consequently, modifications were introduced to the control procedure to align with the constraints imposed by the laboratory hardware configuration. In this subsection, we briefly review the measurement procedure, following the procedure in [15] to acquire the d-q 2D flux-map data points. The well-known d-q equations in the rotor reference frame are given as [19]

$$\begin{cases} \dot{\phi}_q &= -R_s I_q - \omega_e \phi_d + V_q, \\ \dot{\phi}_d &= -R_s I_d + \omega_e \phi_q + V_d, \end{cases} \tag{13}$$

where ϕ_q and ϕ_d denote the q- and d-axis flux linkages, R_s is the stator resistance, I_q and I_d are the q- and d-axis currents, V_q and V_d are the q- and d-axis applied voltages and ω_e is the electrical angular frequency. Under steady-state conditions, (13) simplifies to

$$\begin{cases} \phi_d &= \frac{-R_s I_q + V_q}{\omega_e}, \\ \phi_q &= -\left(\frac{-R_s I_d + V_d}{\omega_e}\right). \end{cases} \tag{14}$$

The flux maps are generated by dividing the d- and q-axis current ranges into a regularly spaced grid and acquiring the flux linkage at each grid point. This current grid can be defined as

$$\begin{cases} I_{d,k} &= I_{d_{min}} + k \cdot \Delta I_d \quad k = 0, \cdots, n, \\ I_{q,l} &= I_{q_{min}} + l \cdot \Delta I_q \quad l = 0, \cdots, n. \end{cases} \tag{15}$$

Here, ΔI_d and ΔI_q specify the step sizes of the grid that are defined by

$$\begin{cases} \Delta I_d &= \frac{I_{d_{max}} - I_{d_{min}}}{n}, \\ \Delta I_q &= \frac{I_{q_{max}} - I_{q_{min}}}{n}, \end{cases} \tag{16}$$

where $I_{d_{min}}, I_{q_{min}}$ specify the minimum d- and q-axis currents, respectively; $I_{d_{max}}, I_{q_{max}}$ specify the maximum d- and q-axis currents, respectively; and n determines the size of the flux map grid. A large n produces a finer grid that captures smaller variations in the flux map at the cost of time spent constructing the flux map.

To maintain the steady-state condition required to simplify (13),

1) The motor under test is driven at constant speed using a speed-controlled servomotor.
2) The motor under test is current controlled at a particular current grid point.

Considering the rated current of the IPM and with a view to capture nonlinear flux variation, we take $I_{d_{min}} = 0, I_{q_{min}} = 0$, $I_{d_{max}} = 10, I_{q_{max}} = 10$ and $n = 40$. Thus the current grid has 41×41 entries with grid spacing calculated using (16) to be $\Delta I_q = \Delta I_d = 0.25$ A.

At each grid point, a current pulse reference is specified for a short time duration T_a. T_a is taken to be approximately 5 times as long as the time needed to complete one mechanical rotation at the specified servomotor speed. This allows for the current transient response to settle and reach steady state. The flux linkages are calculated using voltage and current measurements averaged across one mechanical period. This eliminates harmonic effects and any influence of mechanical defects. Following the pulse reference, the motor is allowed to idle for some time T_i to ensure that motor temperature remains stable. We take $T_i = 2T_a$. In our experiments, the load motor is commanded to regulate shaft speed at 600 rpm, one third of the IPM's rated speed such that the flux map at full rated motor current can be explored. Since one mechanical rotation at this speed takes 0.1 s, T_a is set to be 0.5 s and thus T_i is set to be 1 s.

To calculate the flux linkages using (14), the three-phase currents I_a, I_b, and I_c are measured and converted into d- and q-axis currents. The angle required to perform the transform is inferred using a linear flux observer. The stator resistance value R_s is taken to be the nominal value available on the motor specification plate. Voltages V_q and V_d are calculated by the current controller. ω_e is inferred from the angular speed of the speed-controlled servomotor as $\omega_e = p\omega_r$, where p is the number of pole pairs for the IPM and ω_r is the commanded servomotor speed. Although the experimental results included in this work are limited to the first quadrant, the measurement and reconstruction procedure can be readily extended to other d-q quadrants.

C. Results and Discussion

To acquire the flux map using the CS-based algorithm proposed in this paper, flux linkages at a randomly sampled fraction of the current grid defined in (15) are acquired using the procedure described above. The resulting partial flux maps are denoted by ϕ_p (with q- and d-axis components ϕ_{qp} and ϕ_{dp}, respectively).

Figs. 4(a) and 4(b) show examples of commanded current pulses (red line) and the measured currents (blue line) at the current grid point given by $I_d = 3$ A, $I_q = 4$ A. Figs. 4(c) and 4(d) show the corresponding d- and q-axis voltages commanded by the controller. As mentioned in subsection IV-B, to compute the flux map entry at that grid, the voltage and current measurements are averaged over 0.1 s, corresponding to one full mechanical rotation period. Since the active pulse time $T_a = 0.5$ s, the 0.1 s window starts 0.3 s after the beginning of the pulse to allow for steady state. Eq. (14) is then used to compute the d- and q-axis flux at the current grid point under consideration.

Figs. 5(a) and 5(b) show the flux-linkage data acquired from 25% randomly selected samples of the 41×41 (I_d, I_q) grid. Figs. 5(c) and 5(d) show the corresponding q- and d-axis flux maps constructed using the CS algorithm.

For comparison, the full flux map was acquired at each grid point by using (14). Figs. 6(a) and 6(b) show q- and d-axis flux maps acquired from full-grid experiments, respectively. It can be seen that while the q-axis flux map is nearly linear, the d-axis flux map exhibits significant saturation and cross-saturation behavior. These flux maps serve as the benchmark to compare the flux map acquired using the CS-based algorithm proposed in this paper.

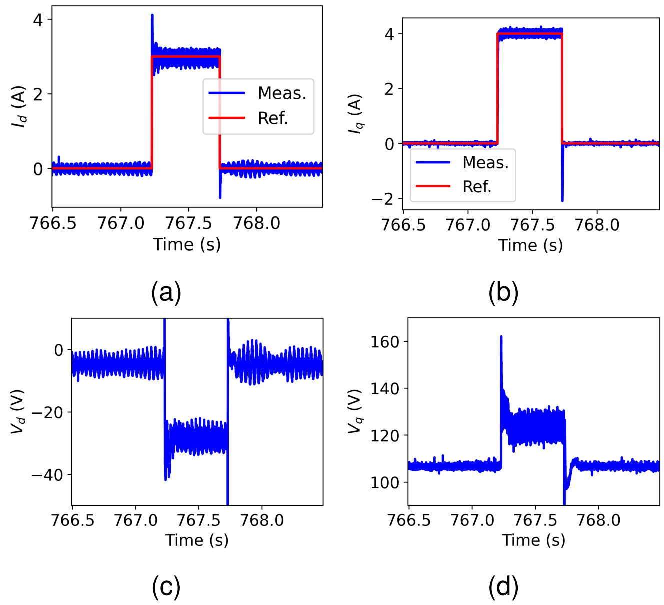

Fig. 4: d- and q-axis current measurements and applied voltages at the grid point defined by $I_d = 3$ A, $I_q = 4$ A. (a) Example d-axis current pulse. (b) Example q-axis current pulse. (c) V_d voltage applied by the controller. (d) V_q voltage applied by the controller.

To visualize the cross-saturation effects, we plot 2D contour maps on the I_d-I_q plane. Fig. 7 shows the true flux-map contours and Fig. 8 shows the reconstructed flux-map contours.

Comparing Fig. 6(a) with Fig. 5(c) and Fig. 6(b) with Fig. 5(d), the absolute errors between the full-grid flux maps and CS-based flux maps for the q- and d-axes are shown in Figs. 9(a) and 9(b), respectively. For comparison, the same flux-axis scale is used for Figs. 5(c) and 9(a) and for Figs. 5(d) and 9(b), respectively. The reconstruction errors remain small across the entire flux map. Further quantitative analysis shows that the RMSE for the d-axis flux map using CS is 0.004 and that for the q-axis flux map is 0.001. Thus, it can be concluded that the 2D flux maps for the Marathon Motors IPM machine can be reconstructed accurately with only 25% randomly selected samples. Consequently, the acquisition time is reduced to approximately one quarter of that required for the full-grid flux maps. Moreover, the proposed algorithm provides a Fourier-domain representation of the flux maps. This representation also enables efficient computation of derivatives of ϕ_d and ϕ_q with respect to I_d and I_q. These derivatives are crucial for calculating maximum-torque-per-ampere (MTPA) control.

V. Conclusion

In this paper, a compressed-sensing (CS)-based approach to magnetic flux map acquisition is proposed for reconstructing 2D and 3D flux maps. Using limited random samples, simulation studies show that flux maps can be reconstructed by leveraging their sparsity in a Fourier basis. Experimental results demonstrate that the proposed method achieves low

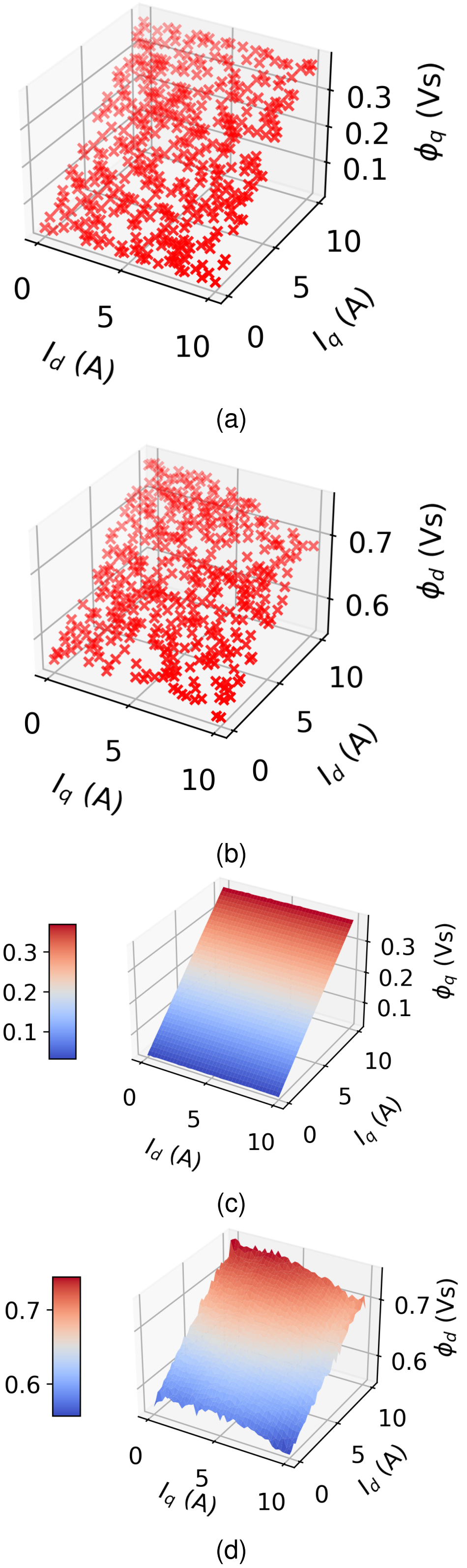

Fig. 5: q- and d-axis flux-map acquisition using the proposed method on Marathon Motors IPM. (a) Randomly sampled ϕ_q data points. (b) Randomly sampled ϕ_d data points. (c) ϕ_q reconstructed using compressed sensing. (d) ϕ_d reconstructed using compressed sensing.

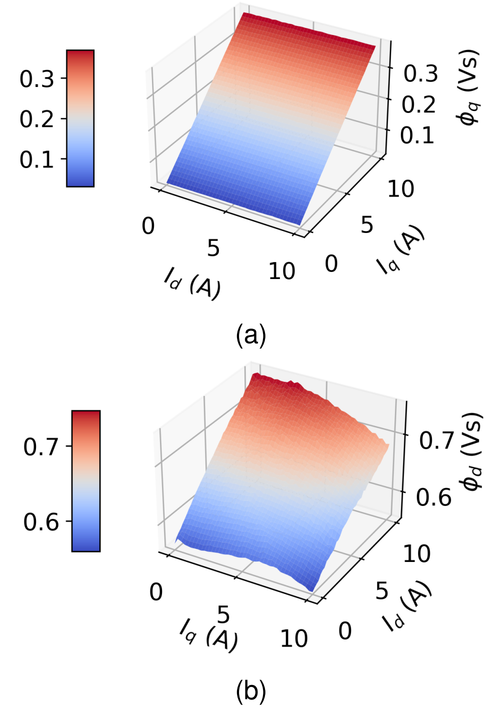

Fig. 6: Full q- and d-axis flux maps using extensive experimental data. (a) True ϕ_q. (b) True ϕ_d.

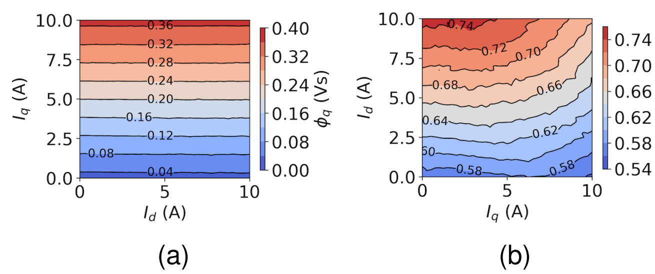

Fig. 7: Full q- and d-axis flux-map contour plots. (a) True ϕ_q. (b) True ϕ_d.

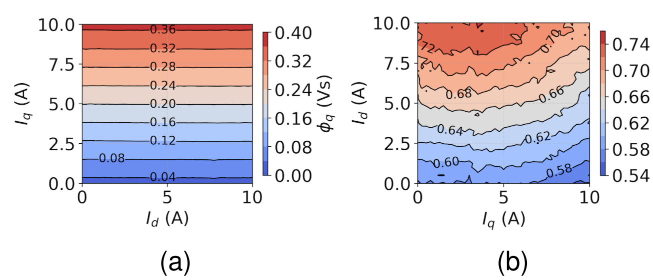

Fig. 8: Reconstructed q- and d-axis flux-map contour plots. (a) reconstructed ϕ_q. (b) reconstructed ϕ_d.

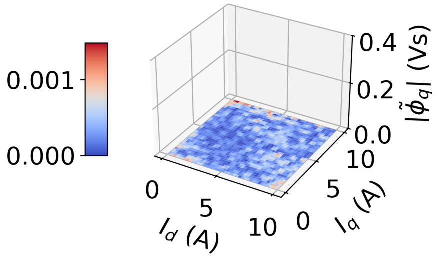

(a)

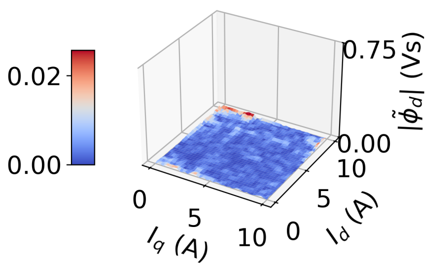

(b)

Fig. 9: Error maps of CS-based reconstructions: (a) q-axis reconstruction error. (b) d-axis reconstruction error.

RMSEs using only 25% of the full experimental samples, thereby substantially reducing acquisition time.

REFERENCES

[1] Q. Liu and K. Hameyer, "High-performance adaptive torque control for an IPMSM with real-time MTPA operation," *IEEE Transactions on Energy Conversion*, vol. 32, DOI 10.1109/TEC.2016.2633302, no. 2, pp. 571–581, 2017.

[2] C. Jia, X. Wang, Y. Liang, and K. Zhou, "Robust current controller for IPMSM drives based on explicit model predictive control with online disturbance observer," *IEEE Access*, vol. 7, DOI 10.1109/ACCESS.2019.2908383, pp. 45 898–45 910, 2019.

[3] J. Lee, Y.-C. Kwon, and S.-K. Sul, "Signal-injection sensorless control with tilted current reference for heavily saturated ipmsms," *IEEE Transactions on Power Electronics*, vol. 35, DOI 10.1109/TPEL.2020.2984029, no. 11, pp. 12 100–12 109, 2020.

[4] J. Lee, Y.-C. Kwon, and S.-K. Sul, "Identification of IPMSM flux-linkage map for high-accuracy simulation of IPMSM drives," *IEEE Transactions on Power Electronics*, vol. 36, DOI 10.1109/TPEL.2021.3084558, no. 12, pp. 14 257–14 266, 2021.

[5] X. Chen, J. Wang, B. Sen, P. Lazari, and T. Sun, "A high-fidelity and computationally efficient model for interior permanent-magnet machines considering the magnetic saturation, spatial harmonics, and iron loss effect," *IEEE Transactions on Industrial Electronics*, vol. 62, DOI 10.1109/TIE.2014.2388200, no. 7, pp. 4044–4055, 2015.

[6] P. Guglielmi, M. Pastorelli, and A. Vagati, "Cross-saturation effects in IPM motors and related impact on sensorless control," *IEEE Transactions on Industry Applications*, vol. 42, DOI 10.1109/TIA.2006.882646, no. 6, pp. 1516–1522, 2006.

[7] B. Stumberger, G. Stumberger, D. Dolinar, A. Hamler, and M. Trlep, "Evaluation of saturation and cross-magnetization effects in interior permanent-magnet synchronous motor," *IEEE Transactions on Industry Applications*, vol. 39, DOI 10.1109/TIA.2003.816538, no. 5, pp. 1264–1271, 2003.

[8] N. Bianchi and S. Bolognani, "Magnetic models of saturated interior permanent magnet motors based on finite element analysis," in *Conference Record of 1998 IEEE Industry Applications Conference. Thirty-Third IAS Annual Meeting (Cat. No.98CH36242)*, vol. 1, DOI 10.1109/IAS.1998.732255, pp. 27–34 vol.1, 1998.

[9] A. Vagati, M. Pastorelli, F. Scapino, and G. Franceschini, "Impact of cross saturation in synchronous reluctance motors of the transverse-laminated type," *IEEE Transactions on Industry Applications*, vol. 36, no. 4, pp. 1039–1046, 2000.

[10] L. Ortombina, F. Tinazzi, and M. Zigliotto, "Magnetic modeling of synchronous reluctance and internal permanent magnet motors using radial basis function networks," *IEEE Transactions on Industrial Electronics*, vol. 65, DOI 10.1109/TIE.2017.2733502, no. 2, pp. 1140–1148, 2018.

[11] N. Bedetti, S. Calligaro, and R. Petrella, "Stand-still self-identification of flux characteristics for synchronous reluctance machines using novel saturation approximating function and multiple linear regression," *IEEE Transactions on Industry Applications*, vol. 52, DOI 10.1109/TIA.2016.2535413, no. 4, pp. 3083–3092, 2016.

[12] Z. Qu, T. Tuovinen, and M. Hinkkanen, "Inclusion of magnetic saturation in dynamic models of synchronous reluctance motors," in *2012 XXth International Conference on Electrical Machines*, DOI 10.1109/ICElMach.2012.6349997, pp. 994–1000, 2012.

[13] M. Hinkkanen, P. Pescetto, E. Mölsä, S. E. Saarakkala, G. Pellegrino, and R. Bojoi, "Sensorless self-commissioning of synchronous reluctance motors at standstill without rotor locking," *IEEE Transactions on Industry Applications*, vol. 53, DOI 10.1109/TIA.2016.2644624, no. 3, pp. 2120–2129, 2017.

[14] G. Bramerdorfer, S. M. Winkler, M. Kommenda, G. Weidenholzer, S. Silber, G. Kronberger, M. Affenzeller, and W. Amrhein, "Using FE calculations and data-based system identification techniques to model the nonlinear behavior of PMSMs," *IEEE Transactions on Industrial Electronics*, vol. 61, DOI 10.1109/TIE.2014.2303785, no. 11, pp. 6454–6462, 2014.

[15] E. Armando, R. I. Bojoi, P. Guglielmi, G. Pellegrino, and M. Pastorelli, "Experimental identification of the magnetic model of synchronous machines," *IEEE Transactions on Industry Applications*, vol. 49, no. 5, pp. 2116–2125, 2013.

[16] A. Patkar, D. Liu, Y. Wang, and K. Y. Toumi, "Magnetic flux map acquisition using a compressed sensing method," in *2024 IEEE 19th Conference on Industrial Electronics and Applications (ICIEA)*, DOI 10.1109/ICIEA61579.2024.10665180, pp. 1–6, 2024.

[17] S. L. Brunton and J. N. Kutz, *Data-Driven Science and Engineering: Machine Learning, Dynamical Systems, and Control*. Cambridge University Press, 2019.

[18] G. P. Simone Ferrari. Synchronous reluctance evolution (SyR-e). [Online]. Available: https://github.com/SyR-e/syre_public

[19] P. Pillay and R. Krishnan, "Modeling, simulation, and analysis of permanent-magnet motor drives. i. the permanent-magnet synchronous motor drive," *IEEE Transactions on Industry Applications*, vol. 25, DOI 10.1109/28.25541, no. 2, pp. 265–273, 1989.

BIOGRAPHIES

Abhishek Patkar received his M.S. and Ph.D. degrees in Mechanical Engineering at the Massachusetts Institute of Technology (MIT) in 2020 and 2025, respectively. He holds a B.S. in Mechanical Engineering and Electrical Engineering from the University of Illinois at Urbana-Champaign in 2018. His research interests include nonlinear, adaptive control, system modeling, identification and learning systems with applications to mechatronic systems.

Yebin Wang (S'06-M'10-SM'16) received his Ph.D. in Electrical Engineering from the University of Alberta, Edmonton, Canada, in 2008. Dr. Wang has been with Mitsubishi Electric Research Laboratories in Cambridge, MA, USA, since 2009, and now is a Senior Principal Research Scientist/Senior Team Leader. His research interests include nonlinear control and estimation, optimal control, adaptive and learning systems, and their applications including mechatronic systems. He is the co-author of over 100 papers in the field of Control and System, and the co-inventor of over 40 US patent applications. He was/is an editorial board member of multiple international journals and conferences.

Abraham Goldsmith received his M.S. degree from Worcester Polytechnic Institute, in 2008. Since 2009, he has been with Mitsubishi Electric Research Laboratories, Cambridge, MA, where he is a Principal Research Scientist. He has worked in areas ranging from wireless sensor networks, optical metrology, NC machines, control, and block chain. Recently, he has focused primarily on the computational aspects of advanced control algorithms for embedded control systems and design automation for embedded systems.

Dehong Liu (S'01-M'03-SM'08) received his B.S., M.S., and Ph.D. degrees all in electrical engineering from Tsinghua University, Beijing, China, in 1997, 1999, and 2002, respectively. From 2003 to 2010, he was with the Department of Electrical and Computer Engineering, Duke University, Durham, NC, USA, first as a Research Associate and then as a Senior Research Scientist. Since 2010, he has been with Mitsubishi Electric Research Laboratories (MERL), Cambridge, MA, USA, where he is now a Lead Research Scientist. His current research interests include electric machine fault diagnosis, electromagnetic compatibility, signal processing, and machine learning.

Kamal Youcef-Toumi is a Professor of Mechanical Engineering at the Massachusetts Institute of Technology (MIT). He holds a B.S. from the University of Cincinnati and both M.S. and Sc.D. degrees from MIT. Youcef-Toumi's fundamental research centers on system dynamics modeling, design methodologies, control theory, and computational intelligence. His applications span robotics, automation, and intelligent systems. He is an IEEE Senior member, an ASME Fellow, and a Fellow of the International Association of Advanced Materials.